PLOS ONE

RESEARCH ARTICLE

Structural characterization of two nanobodies targeting the ligand-binding pocket of human Arc

José M. Godoy Muñoz[1], Lasse Neset[1], Sigurbjörn Markússon[1], Sarah Weber[1], Oda C. Krokengen[1], Aleksi Sutinen[2], Eleni Christakou[1], Andrea J. Lopez[1], Clive R. Bramham[1], Petri Kursula[1,2]*

1 Department of Biomedicine, University of Bergen, Bergen, Norway, **2** Faculty of Biochemistry and Molecular Medicine & Biocenter Oulu, University of Oulu, Oulu, Finland

* petri.kursula@uib.no

Citation: Godoy Muñoz JM, Neset L, Markússon S, Weber S, Krokengen OC, Sutinen A, et al. (2024) Structural characterization of two nanobodies targeting the ligand-binding pocket of human Arc. PLoS ONE 19(4): e0300453. https://doi.org/10.1371/journal.pone.0300453

Editor: Parvez Alam, National Institutes of Health, UNITED STATES

Received: November 3, 2023

Accepted: February 27, 2024

Published: April 29, 2024

Data Availability Statement: The crystallographic data presented in this manuscript are available at the Protein Data Bank with the following accession numbers: 8QF3 (nanobody H11; https://doi.org/10.2210/pdb8QF3/pdb), 8QF4 (Arc-NL bound to nanobody H11; https://doi.org/10.2210/pdb8QF4/pdb), 8QF5 (Arc-NL bound to nanobody E5; https://doi.org/10.2210/pdb8QF5/pdb).

Funding: The Core Facility for Biophysics, Structural Biology, and Screening (BiSS) at the University of Bergen has received infrastructure

Abstract

The activity-regulated cytoskeleton-associated protein (Arc) is a complex regulator of synaptic plasticity in glutamatergic neurons. Understanding its molecular function is key to elucidate the neurobiology of memory and learning, stress regulation, and multiple neurological and psychiatric diseases. The recent development of anti-Arc nanobodies has promoted the characterization of the molecular structure and function of Arc. This study aimed to validate two anti-Arc nanobodies, E5 and H11, as selective modulators of the human Arc N-lobe (Arc-NL), a domain that mediates several molecular functions of Arc through its peptide ligand binding site. The structural characteristics of recombinant Arc-NL-nanobody complexes were solved at atomic resolution using X-ray crystallography. Both anti-Arc nanobodies bind specifically to the multi-peptide binding site of Arc-NL. Isothermal titration calorimetry showed that the Arc-NL-nanobody interactions occur at nanomolar affinity, and that the nanobodies can displace a TARPγ2-derived peptide from the binding site. Thus, both anti-Arc-NL nanobodies could be used as competitive inhibitors of endogenous Arc ligands. Differences in the CDR3 loops between the two nanobodies indicate that the spectrum of short linear motifs recognized by the Arc-NL should be expanded. We provide a robust biochemical background to support the use of anti-Arc nanobodies in attempts to target Arc-dependent synaptic plasticity. Function-blocking anti-Arc nanobodies could eventually help unravel the complex neurobiology of synaptic plasticity and allow to develop diagnostic and treatment tools.

Introduction

The mammalian brain is a complex integrator of multisensory information that can coordinate behavioral responses and promote environmental adaptation. Memory and learning are essential in survival, as they mediate the integration, stabilization and retrieval of new information, thereby guiding behavior in an adaptative manner [1]. Concurrently, neurobiological studies have shown that memory and learning are mediated by the reorganization of synaptic circuits,

funding from the Research Council of Norway through NORCRYST (grant number 245828) and NOR–OPENSCREEN (grant number 245922). The funders had no role in study design, data collection and analysis, decision to publish, or preparation of the manuscript.

Competing interests: The authors have declared that no competing interests exist.

whereby individual neurons selectively modulate the strength of their synapses through synaptic plasticity [2–5].

Plastic changes in synaptic strength involve tightly regulated molecular pathways that can rapidly respond to local variations in neuronal activity [6]. A major regulator of synaptic plasticity is the activity-dependent cytoskeleton-associated protein (Arc). Arc is predominantly expressed in neocortical and hippocampal non-GABAergic CaMKIIα-positive glutamatergic neurons of rats [7]. Hence, Arc has been associated with the regulation of long-term memory and learning in the mammalian brain [8–10]. Arc is essential for the consolidation of different types of memory, playing a key role in the stabilization of memory-associated neural circuitry [11–13]. Furthermore, Arc has been associated with stress regulation [14,15], sleep homeostasis [16,17], and Alzheimer's disease [18–22], as well as other neurological and psychiatric disorders [23–25].

The involvement of Arc in physiological and pathological processes has led to an increased interest in the structure and molecular mechanisms of Arc. Arc has critical roles in several major forms of synaptic plasticity: N-methyl-D-aspartate receptor (NMDAR)-dependent long-term potentiation (LTP) and long-term depression (LTD), metabotropic glutamate receptor (mGluR)-dependent LTD as well as homeostatic synaptic scaling [reviewed in 8,23]. Therefore, Arc can increase or reduce the synaptic strength of specific synapses (in NMDAR-dependent LTP and mGluR-dependent LTD) and of all the excitatory synapses of a neuron (in synaptic scaling). These molecular mechanisms are only partially understood.

In the postsynaptic compartment of dendritic spines, Arc facilitates endocytosis of α-amino-3-hydroxy-5-methyl-4-isoxazolepropionic acid receptors (AMPAR) during mGluR-dependent LTD and synaptic scaling [26,27] and promotes actin cytoskeletal remodeling in NMDAR-dependent LTP [28]. In addition, Arc enters the nucleus and regulates gene transcription [29,30] The functional complexity of Arc is further highlighted by its ability to form reversible oligomeric states [31–35]. Arc can oligomerize into virus-like capsids containing *Arc* mRNA that can be transferred to neighboring cells [36]. Capsid formation is explained by the retroviral origin of Arc as a repurposed retrotransposon, but the molecular structure and assembly of mammalian Arc capsids is unknown [32,36,37]. Overall, the variety of interrelated molecular functions emphasizes the need to further characterize Arc on a structural and functional level.

Structural biology has provided considerable insights into the functional complexity of Arc, which can be divided into two main protein domains with different functions (Fig 1). An oligomerization motif has been traced to the Arc N-terminal domain (NTD) [38], within the second coil of a predicted antiparallel coiled-coil. The Arc C-terminal domain, also called the capsid domain, has structural homology to retroviral GAG. The Arc-CTD is a bilobar domain comprised an N-lobe (NL) and C-lobe (CL). The Arc-NL binds peptides of several postsynaptic interaction partners, including the transmembrane AMPAR regulatory protein γ2 (TARPγ2, also known as stargazin), implicated ion synaptic anchoring and trafficking of AMPAR [37].

The high-resolution structure of full-length Arc (flArc) remains unknown, as the molecular flexibility of Arc hinders crystallization [34]. To face this problem, anti-Arc nanobodies have been developed and used as crystallization chaperones for the rat and human Arc C-terminal domain (Arc-CTD) [40,42]. Isothermal titration calorimetry (ITC) revealed that the anti-Arc nanobody H11 can displace a TARPγ2-derived peptide from the multi-peptide binding pocket of flArc, suggesting an application for this nanobody as a functional modulator of Arc function [40]. There is therefore increased interest in anti-Arc nanobodies that selectively bind Arc-NL.

To support the potential applications of anti-Arc-NL nanobodies, we characterized the structural and functional properties of protein complexes formed between Arc-NL and the

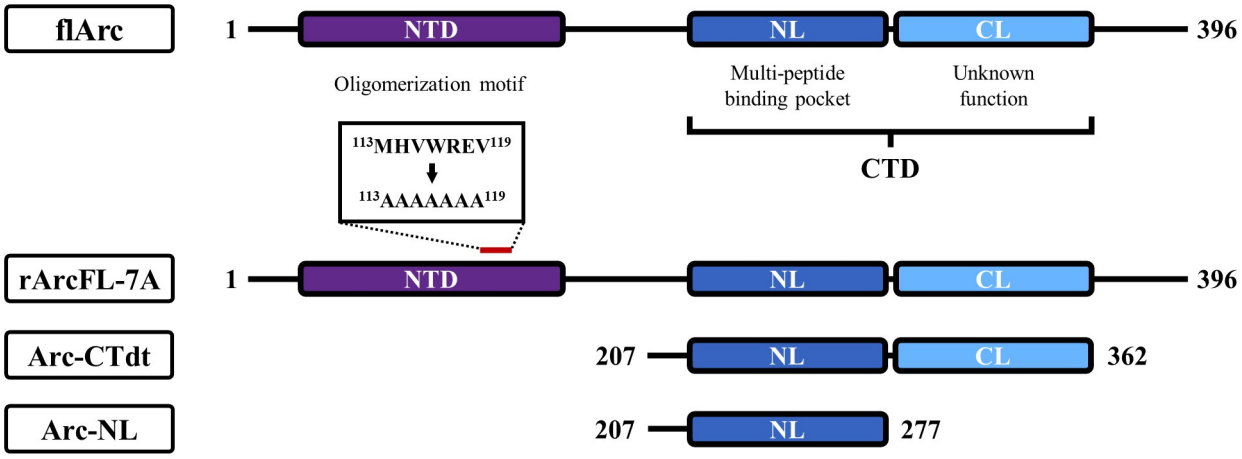

Fig 1. Domains of full-length Arc and recombinant Arc constructs. Full-length Arc (flArc) is constituted by two main domains: The N-terminal domain (NTD) and the C-terminal domain (CTD). Arc-NTD contains the oligomerization motif, while the Arc-CTD can be further divided into the N-lobe (NL) and the C-lobe (CL). Arc-NL contains a multi-peptide binding pocket that mediates several of the molecular functions of Arc [39–41]. This study used three recombinant Arc constructs: Dimeric full-length Arc (rArcFL-7A), Arc-CTD without its C-terminal tail (Arc-CTdt) and Arc-NL. The N-terminal histidine-tags, fusion proteins and linker regions of the recombinant proteins are not shown in this figure.

https://doi.org/10.1371/journal.pone.0300453.g001

anti-Arc nanobodies E5 and H11. Both nanobodies bound to the multi-peptide binding pocket of Arc-NL, which validates them as possible functional modulators of Arc-NL. Nanobody E5 bound flArc simultaneously with nanobody C11, which targets the Arc C-lobe [40,42]. These findings open a path towards using anti-Arc-NL nanobodies to characterize the different structural states and complex molecular functions of the Arc protein.

Materials and methods

Materials

All chemicals were acquired from Sigma-Aldrich (Merck Group; Massachusetts, US) and all other materials from Thermo Fisher Scientific (Massachusetts, US), unless otherwise specified. For crystal picking, 50-200 μm MicroLoops LD (MiTeGen, Ithaca, New York, US) were used. FITC-labelled, TAT-tagged TARPγ2 peptides (forward peptide P1: `YGRKKRRQRRRGGRIPSYRYR`, reverse peptide P2: `YGRKKRRQRRRGGRYRYSPIR`) were obtained from GenScript Biotech (Piscataway, New Jersey, US).

Expression constructs

Five recombinant protein constructs were used in this study: anti-Arc nanobody E5, anti-Arc nanobody H11, Arc-NL ($Arc_{207-277}$; identical for human, rat and mouse Arc-NL), rArcFL-7A full-length dimer, and human Arc-CTD without the C-terminal tail (Arc-CTdt, residues 206-361). The recombinant Arc constructs are displayed in Fig 1. Anti-Arc nanobodies H11 and E5 were generated in alpacas as described [40,42] and provided by Nanotag Biotechnologies (Göttingen, Germany) in prokaryotic pNT1433 expression vectors. The recombinant nanobodies carried an N-terminal histidine-tag followed by a tobacco etch virus (TEV) protease cleavage site (His_6-TEV-E5/H11). The Arc-NL construct was in a prokaryotic pETMBP_1a expression vector fused with maltose binding protein (His_6-MBP-TEV-NL) [34]. The full-length rat Arc construct containing a poly-Ala mutation in residues 113-119 (rArcFL-7A) was expressed with an N-terminal fusion (His_6-MBP) in a pHMGWA vector [43]. Arc-CTdt was expressed using the pTH27 vector [44].

Recombinant protein expression and purification

All recombinant proteins were expressed in *E. coli* and purified as described [39,40]. Briefly, all proteins were expressed in BL21(DE3) *E. coli* and purified using nickel-nitrilotriacetic acid (Ni-NTA) affinity chromatography. After proteolytic cleavage of the tag and dialysis, reverse Ni-NTA chromatography was conducted to remove His-tagged contaminants. For rArcFL-7A, an amylose affinity chromatography step was additionally included. For size exclusion chromatography (SEC), the sample was concentrated and applied to a HiLoad 16/600 Superdex 75 pg or a HiLoad 16/60 Superdex 200 pg column (GE Healthcare, Illinois, US). The purity of each protein fraction was assessed through SDS-PAGE; the purest fractions were pooled, concentrated, and snap-frozen for storage at -80 ˚C. Protein concentration was measured with a NanoDrop 2000 spectrophotometer (Thermo Scientific, Massachusetts, US) or with an Abbemat Performance 500 Refractometer (Anton Paar GmbH, Graz, Austria).

Dynamic light scattering (DLS)

DLS was performed using Zetasizer Nano ZS (Malvern Panalytical, Malvern, UK). Samples were filtered using an Ultrafree-MC-GV Centrifugal Filter (Durapore-PVDF, 0.22 μm) (Merck KGaA, Darmstadt, Germany), diluted to 2 mg/ml of protein in 40 μl and loaded into a quartz precision cell (light path: 3x3 mm; Z-height: 8.5 mm) (Hellma, Müllheim, Germany). DLS measurements were taken at 4 ˚C with a pre-incubation period of 60-120 s. Three measurements of each sample were taken (12 runs/measurement, 10 s/run).

Circular dichroism (CD) spectroscopy

CD spectroscopy was performed using a Jasco J-810 spectropolarimeter (Jasco, Tokyo, Japan). Before each experiment, the samples were dialyzed overnight against 10 mM phosphate buffer (pH 7.5) and filtered with Ultrafree-MC-GV centrifugal filters (Durapore-PVDF, 0.22 μm) (Merck KGaA, Darmstadt, Germany). Filtered samples containing 0.15-0.20 mg/ml of protein were loaded into a 1-mm quartz cuvette (Hellma, Müllheim, Germany). CD spectra were measured at 20 ˚C in continuous scanning mode using the following parameters: spectral width 185-280 nm; standard sensitivity 100 mdeg; scan speed 50 nm/min; data pitch 1 nm; 4 s response; bandwidth 1 nm. Each run consisted of the accumulation of four individual spectra, and buffer spectra were subtracted.

The CD spectra were analyzed using CDToolX (v2.01, Birkbeck College, University of London) [45]. The raw ellipticity units (mdeg) were converted into $\Delta\varepsilon$ (M^{-1} cm^{-1}).

Synchrotron radiation circular dichroism (SRCD) spectroscopy

High-resolution SRCD spectra were measured on the AU-CD beamline at the synchrotron storage ring ASTRID2 (ISA, Aarhus, Denmark), using 0.15-0.20 mg/ml protein samples dialyzed and filtered as above. 30 μl of sample were loaded into a 0.1-mm pathlength closed circular cuvette (Hellma, Müllheim, Germany). SRCD spectra were measured at 25 ˚C using a wavelength range of 170-280 nm. Each run consisted of the accumulation of six individual spectra.

Heat stability of the target protein is expected to increase upon binding to a nanobody. To determine the denaturation midpoint (T_m) of each protein sample, temperature scans were carried out by measuring the CD spectrum of each sample between 24.2-84.5 ˚C (heating rate 2.5 ˚C/min). The ellipticity values at 208 nm (for Arc-NL, Arc-NL-E5 and Arc-NL-H11) and 190 nm (for E5 and H11) were chosen as indicators of folding state. Assuming a two-state denaturation process (Folded protein [F] → Unfolded protein [U]), the ellipticity values were

transformed to represent the fraction of unfolded protein [46]. Then, the T_m of each protein was calculated by fitting the data to a sigmoidal curve using the Boltzmann sigmoidal function in GraphPad Prism (v9.5.1).

CD spectral deconvolution

Individual CD and SRCD spectra were averaged in CDToolX [45]. The averaged datasets were uploaded to BeStSel [47]. Deconvolution was performed using a scale factor of 1 for several wavelength ranges. The deconvolution profile with the lowest associated root-mean-squared deviation factor (RMSD) was chosen as the optimal profile [48,49].

Protein crystallization

Protein crystallization was carried out using the sitting drop method for anti-Arc nanobody H11, Arc-NL in complex with E5, and Arc-NL in complex with H11. Multiple crystallization conditions were tested using the commercial screens JCSG+ and PACT Premier (Molecular Dimensions, Sheffield, UK) at two temperatures (8 ˚C and 20 ˚C) in 96-well sitting drop iQ plates (STP Labtech, Melbourn, UK). The Arc-NL-nanobody complexes were formed by directly mixing equimolar amounts of each protein (for Arc-NL-E5) or a 1.5-fold excess of nanobody (for Arc-NL-H11). Protein samples (6-9 mg/ml) were plated using a Mosquito LCP crystallization robot (SPT Labtech, Melbourn, UK). For each condition, three drops (300 nl) with different protein:mother liquor ratios (2:1, 1:1 and 1:2) were deposited next to a 70 μl reservoir containing the precipitant well solution. The different ratios were a means to locally screen protein and precipitant concentration, effectively starting from three different points in the phase transition diagram at each condition.

All three protein samples produced crystals in the commercial screens. Conditions used for crystal picking, X-ray diffraction, and crystal structure solution are listed below.

H11 (8.7 mg/ml, TBS buffer) crystallized at 8 ˚C in a 300-nl drop with a 1:1 protein:well solution ratio after ~30-60 days. The well solution contained 0.1 M Bis-Tris (pH 5.5) and 25% w/v PEG 3350. The crystal was not cryoprotected during cryocooling.

The Arc-NL-H11 complex (4.2 mg/ml H11, 1.8 mg/ml Arc-NL, TBS buffer) crystallized at 20 ˚C in a 300-nl drop with a 1:2 protein:well solution ratio after ~14 days. The well solution contained 0.1 M potassium phosphate/citrate pH 4.2, 0.2 M NaCl and 20% w/v PEG 8000. The crystal was not cryoprotected.

The Arc-NL-E5 complex (4.1 mg/ml E5, 2.8 mg/ml Arc-NL, TBS buffer) crystallized at 20 ˚C in a 300-nl drop with a 1:1 protein:well solution ratio after ~30 days. The well solution contained 0.1 M Tris pH 8, 0.01 M $ZnCl_2$ and 20% w/v PEG 6000. The crystal was cryoprotected using well solution supplemented with 25% glycerol.

X-ray diffraction data collection and structure determination

Data collection took place on the P11 beamline at the German Electron Synchrotron (DESY, Hamburg, Germany) [50]. The data were collected at 100 K on an Eiger 2X 16M detector with a 50x50 μm^2 focused beam at 25-35% transmission. Images were taken using an oscillation range of 0.1˚ and 10 ms exposure per frame. The data were processed with XDS (v10.01.2022) [51] and evaluated using Xtriage (v1.20.2) [52].

Crystallographic phases were solved via molecular replacement using the structures of anti-Arc nanobody E5 (PDB ID: 7R20) [40] and the Arc-NL bound to a TARPγ2 (stargazin) peptide (PDB ID: 6TNO) [39] as search models. Refinement was carried out in phenix.refine (v1.20.2) [53] and manual model building in Coot (v0.9.8.7) [54]. Data processing and refinement statistics are in Table 1. Structure validation was conducted using MolProbity [55]. The

Table 1. X-ray diffraction data and refinement statistics. Data in parentheses correspond to the highest-resolution shell.

Protein	Arc-NL-H11	Arc-NL-E5	H11
Beamline	P11/DESY	P11/DESY	P11/DESY
Wavelength (Å)	0.83	1.03	1.03
Resolution range (Å)	50–1.02 (1.05-1.02)	50–1.50 (1.54-1.50)	50–1.25 (1.28-1.25)
Space group	$P2_1$	$P22_12_1$	$P4_32_12$
Unit cell parameters	a = 41.82 Å b = 52.07 Å c = 44.22 Å α = γ = 90˚ β = 109.89˚	a = 34.50 Å b = 99.48 Å c = 138.32 Å α = β = γ = 90˚	a = b = 57.17 Å c = 145.64 Å α = β = γ = 90˚
Completeness (%)	95.2 (79.9)	99.5 (99.9)	99.9 (99.7)
Mean I/σ(I)	13.0 (0.8)	15.0 (0.7)	13.1 (0.6)
Wilson B-factor ($Å^2$)	15.4	37.9	25.8
R_{cryst} (%)	5.4 (201.7)	4.9 (287.9)	7.1 (367.9)
$CC_{1/2}$ (%)	99.9 (31.6)	99.9 (31.7)	99.9 (28.2)
R_{work} (%)	12.9	14.5	18.5
R_{free} (%)	16.0	19.3	23.2
RMSD bond lengths(Å)	0.020	0.011	0.018
RMSD bond angles (˚)	1.58	1.10	1.70
Ramachandran favored (%)	98.4	97.3	99.60
Ramachandran outliers (%)	0	0	0
MolProbity score/percentile	$1.25/89^{th}$	$1.19/97^{th}$	$1.22/95^{th}$
PDB code	8QF4	8QF5	8QF3

https://doi.org/10.1371/journal.pone.0300453.t001

analysis of protein interfaces was carried out using PISA (http://www.ebi.ac.uk/pdbe/prot_int/pistart.html) [56]. Molecular representations and structural analyses of protein interfaces were done using UCSF Chimera (v1.17.3) [57] and PyMOL (v2.5.4).

Size exclusion chromatography—Multi-angle light scattering (SEC-MALS)

SEC-MALS was performed to estimate the oligomeric state and stoichiometry of the rArcFL7A dimer and its nanobody complexes. SEC was performed on a HiLoad 16/60 Superdex 200 pg SEC column (GE Healthcare) equilibrated with 20 mM Tris pH 7.5, 150 mM NaCl and 0.5 mM TCEP using a Shimadzu Prominence-i LC-2030C 3D HPLC unit (GMI, MN, USA) with an LC-2030/2040 PDA UV detector (Shimadzu, Kyoto, Japan). The system was calibrated using bovine serum albumin shortly before running the samples. 50 μg of each protein complex in the running buffer were injected at a flow rate of 0.5 ml/min and light scattering and refractive index were recorded using a miniDAWN TREOS detector (Wyatt Technologies, CA, USA) and a RefractoMax 520 refractometer (Wyatt Technologies). Data collection and SEC-MALS analysis were carried out using ASTRA 6.1 (Wyatt Technologies).

Analytical SEC

To see if the Arc-CTdt (C-terminal domain lacking the disordered tail) construct was in fact able to bind two nanobodies simultaneously and to make sure the complex peak would not overlap with the excess nanobody peaks, a small-scale analytical SEC was run. For each run, 3 nmol Arc-CTdt were used, and the nanobodies H11 and C11 were added in 1.3-fold excess (3.9 nmol). SEC was run on a Superdex 75 increase 10/300 GL column (GE Healthcare), at a flow rate of 0.6 ml/min. The running buffer was 20 mM Tris pH 7.4, 150 mM NaCl.

Small-angle X-ray scattering

In SEC-SAXS, the sample is eluted from the gel filtration column directly into the X-ray beam. Arc and the nanobodies were combined in a 1:1.3 protein-to-nanobody ratio to ensure all the Arc protein is bound to the nanobodies. The proteins were gently mixed and incubated on ice for 1 h. After incubation, the proteins were filtered using an Ultrafree 0.22 μm centrifugal filter (Merck Millipore) to remove any aggregation. For SEC-SAXS, Agilent Bio SEC-3 Column (Agilent Technologies, CA, USA) or HiLoad 16/60 Superdex 200 pg SEC column (GE Healthcare) were used, with 20 mM Tris pH 7.5, 150 mM NaCl and 0.5 mM TCEP as running buffer.

SEC-SAXS data collection was performed twice. First on the CoSAXS beamline [58] at MAX IV (Lund, Sweden) and again on the SWING beamline [59] at the SOLEIL synchrotron (Gif-sur-Yvette, France). The data shown here are from SOLEIL, due to better signal-to-noise ratio and lack of radiation damage. Buffer subtraction and frame selection were performed in CHROMIXS [60], primary analysis in PRIMUS [61] and distance distribution function analysis using GNOM [62]. *Ab initio* model building was done with DAMMIN [63] and GASBOR [64].

Functional assay using ITC

ITC was performed with a MicroCal iTC200 instrument (Malvern Panalytical, Malvern, UK). The temperature was set to 20 ˚C, using a reference power of 5 μcal/s, a stirring speed of 1000 rpm, and a filter period of 5 s. For titration of the nanobodies into Arc-NL, 15 μM E5/H11 (titrant) and 1.5 μM Arc-NL (titrate), both diluted in TBS (20 mM Tris-HCl pH 7.5, 150 mM NaCl), were used. Each titration consisted of a 0.5 μl initial injection followed by 18 injections (2 μl, 4 s each; separated by 120 s). Four high-quality replicates were obtained for each nanobody.

Titration of FITC-labelled TARPγ2 peptide (P1) into Arc-NL (positive control) was conducted with 2 mM P1 (titrant) and 200 μM Arc-NL (titrate), both diluted in TBS. Three sequential titrations were carried out to ensure that saturation was reached at the end of the assay; each titration consisted of a 0.5 μl initial injection followed respectively by 18, 10, and 5 injections (2 μl, 4 s each, separated by 120 s). The three individual data files were concatenated using the ConCat32 tool (provided by the manufacturer) into a single datafile.

Titration of FITC-labelled reverse TARPγ2 peptide (P2) into Arc-NL (negative control) was conducted with 0.5 mM P2 (titrant) and 50 μM Arc-NL (titrate), both diluted in TBS. The titration consisted of one 0.5 μl initial injection followed by 9 injections (4 μl, 8 s each; separated by 240 s).

For the displacement assays, 100 μM E5/H11 (titrant), and a titrate solution of 10 μM Arc-NL saturated with 100 μM P1, were used. Both solutions were diluted in TBS. Each titration consisted of a 0.5 μl initial injection followed by 18 injections (2 μL, 4 s each; separated by 120 s).

ITC data analysis. Data analysis was carried out following a pre-established protocol based on three inter-connected programs [65]. Automatic peak integration and control subtraction were conducted in NITPIC (v2.0.7) [66]. The integrated data were fitted to a sigmoidal curve using a 1:1 binding model in SEDPHAT (v14.1) [67]. SEDPHAT was also used to calculate and subtract (1) the heats of dilution and (2) the heats of ionization of the buffer. After fitting, best-fit values and their 68.3% confidence interval (± σ) were obtained for the binding enthalpy (ΔH) and association constant ($K_A = 1/K_D$). From these values, the best-fit values for binding entropy (ΔS) and free energy (ΔG) were calculated by the software. The graphs shown in S1 Fig were plotted using GUSSI (v1.7.2) [68].

Sequence homology search of the CDR3s of anti-Arc-NL nanobodies

Sequence homology searches were carried out in Protein BLAST [69] using the CDR3 of both anti-Arc-NL nanobodies E5 and H11 as query sequences. The results were restricted to three target species: *Homo sapiens* (taxid:9606), *Rattus norvegicus* (taxid:10116) and *Mus musculus* (taxid:10090). The non-redundant protein sequence database was used. Due to the short length of the query sequence, only matches with an E-value < 100 were studied, and only those with an E-value ≤ 10 were considered relevant. After extracting the sequences, sequence alignment between each CDR3 and selected sequences was performed using Clustal Omega (v1.2.2) [70] and visualized in Jalview (v2.11.3.2) [71].

Results and discussion

Protein characterization

For interaction assays and high-resolution structural studies, Arc-NL and the anti-Arc nanobodies E5 and H11 were purified in high yield. DLS shows that the three samples are monodisperse (Fig 2A). None of the purified proteins show a tendency for aggregation, and their hydrodynamic radii (R_H) correspond to their respective molecular weights (i.e., R_H-Arc-NL [8.9 kDa] $<$ R_H-E5 [12.8 kDa] $<$ R_H-H11 [14.1 kDa]). In addition, rArcFL-7A and Arc-CTdt were purified as previously shown [40].

CD spectra for Arc-NL, E5 and H11 show that all proteins are likely to be correctly folded (Fig 2B–2D). For Arc-NL, the spectra show that the structure is mainly α-helical (Fig 2B and 2D) [72]. For both nanobodies, the ellipticity signal is weak above 210 nm, indicating structural features canceling each other in the spectrum (Fig 2B and 2C). The positive peak at 200 nm is a strong indicator that both nanobodies consist mostly of β-sheets (Fig 2B and 2C). The presence of these secondary structure components and the lack of negative ellipticity at 195 nm (characteristic of disordered proteins) [72] indicate that all proteins are correctly folded. The SRCD spectra of both Arc-nanobody complexes show a negative peak around 208 nm (Fig 2D), further indicating that Arc-NL is folded in solution with both nanobodies. The deconvolution profiles of all CD and SRCD spectra are shown in Table 2.

BeStSel was chosen as the optimal deconvolution software to analyze the nanobody CD spectra, as it is sensitive to different conformations of β-strands [47]. The deconvolution supports a predominance of α-helices in Arc-NL and β-strands in the nanobodies. Altogether, DLS and CD/SRCD spectroscopy show that the recombinant proteins are monodisperse and correctly folded.

SRCD spectroscopy was further used to study the thermal stability of the proteins and complexes. Both complexes have a higher T_m than any of the proteins alone (Fig 2E and 2F; Table 3), although the apparent effect is mild for H11. The Arc-NL-E5 complex shows the highest increase in T_m of 16.1 ˚C. The data show an increase in thermal stability when the nanobodies bind to Arc, and the presence of E5 causes stronger stabilization. A stronger stabilization by H11, and weaker by E5, was observed earlier, when a thermal stability assay was carried out using differential scanning fluorimetry and the full-length rArcFL-7A construct [40]. This comparison suggests additional interactions, especially for H11, in the context of full-length Arc.

Both E5 and H11 interact with the peptide binding pocket of Arc-NL

Crystallization was successful for Arc-NL-H11, Arc-NL-E5 and unbound H11, and structures could be refined at atomic resolution (1.02 Å for Arc-NL-H11, 1.5 Å for Arc-NL-E5 and 1.33 Å for H11). In addition, the crystal structure of apo-E5 had been solved before [40]. The

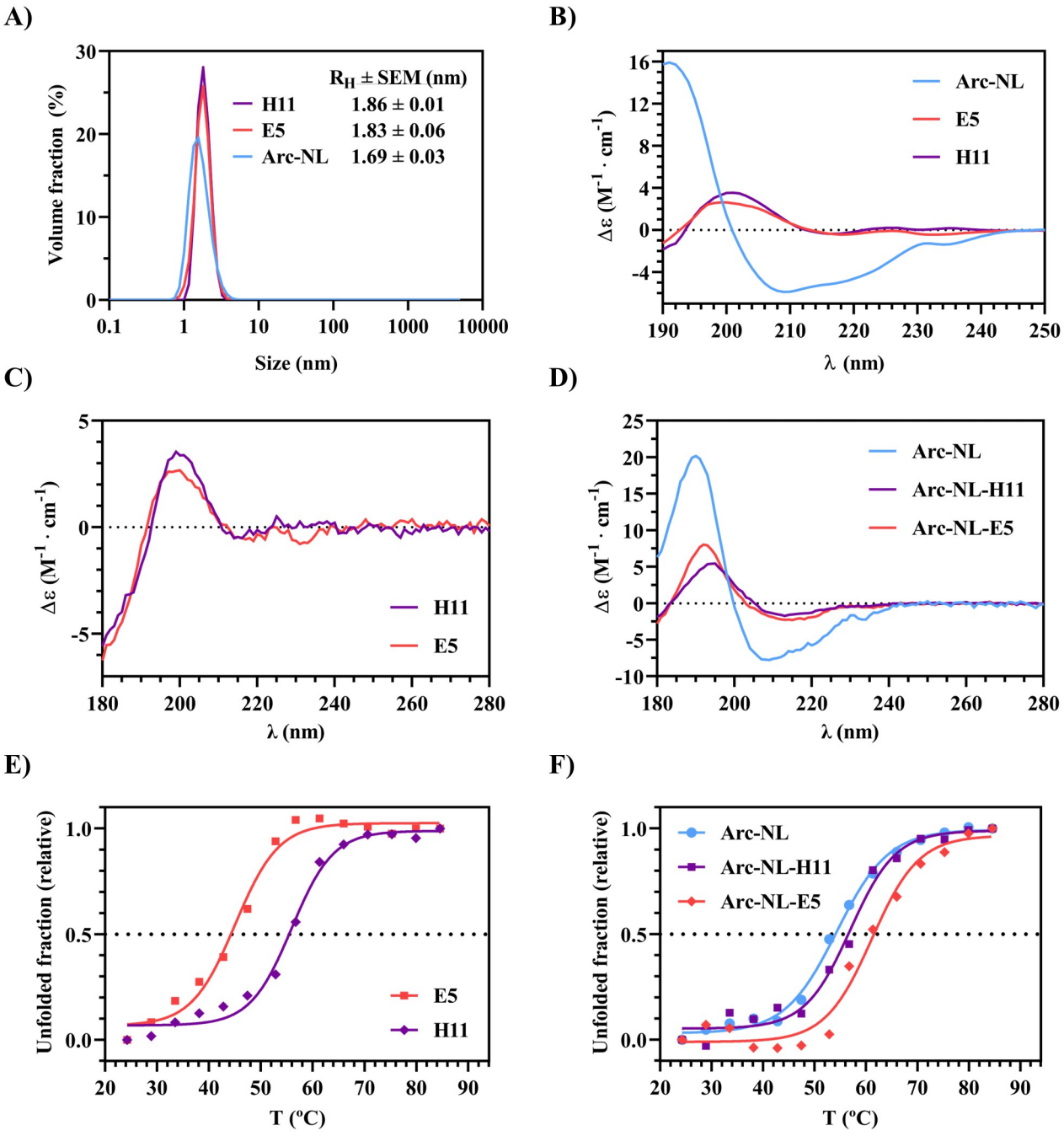

Fig 2. Characterization of Arc-NL, E5 and H11. (A) DLS analysis of Arc-NL, E5 and H11. (B) CD spectroscopy of Arc-NL, E5 and H11. (C) SRCD spectroscopy of H11 and E5. (D) SRCD spectroscopy of Arc-NL, and the Arc-nanobody complexes Arc-NL-H11 and Arc-NL-E5. (E) Thermal denaturation curves based on SRCD of H11 and E5; the analysis is based on ellipticity at 190 nm. (F) Thermal denaturation curves based on SRCD of Arc-NL and the Arc-nanobody complexes Arc-NL-H11 and Arc-NL-E5. The analysis is based on ellipticity at 208 nm.

https://doi.org/10.1371/journal.pone.0300453.g002

crystals that underwent X-ray diffraction are shown in Fig 3A, together with the refined structures (Fig 3B). See Table 1 for detailed X-ray diffraction data and refinement statistics.

A structural analysis of the Arc-nanobody complexes reveals that E5 and H11 both bind the multi-peptide binding site of Arc-NL (Fig 4A). When binding Arc-NL, both E5 and H11

Table 2. Deconvolution profiles of CD/SRCD spectra. Deconvolution was done using BeStSel of Arc-NL, E5, H11, and Arc-nanobody complexes Arc-NL-E5 and Arc-NL-H11. The BeStSel algorithm divides the deconvoluted signals into four main categories of protein secondary structures: α-helices, β-strands, turns and others.

Protein	Experiment	α-helix (%)	β-strand (%)	Turns (%)	Others (%)
Arc-NL	CD	44.1	1.1	6.2	48.6
	SRCD	42.1	3.5	6.3	48.2
E5	CD	0	41.3	16.3	42.4
	SRCD	0	40.6	16.3	43.0
H11	CD	0	55.8	10.7	33.5
	SRCD	0	56.2	9.8	34.0
Arc-NL-E5	SRCD	12.3	29.6	7.9	50.2
Arc-NL-H11	SRCD	14.8	31.4	9.4	44.5

https://doi.org/10.1371/journal.pone.0300453.t002

undergo conformational changes in their CDRs (Fig 4B). Comparing the bound and free forms of the nanobodies indicates that for both E5 and H11, CDR3 shows a conformational change, which involves the orientation of the aromatic residue bound into the peptide-binding pocket of Arc-NL (Fig 4B). The CDR3 of E5 forms a β-sheet with the Arc-NL N-terminal loop when the complex is formed (Fig 4A and 4C), similarly to the TARPγ2 ligand peptide [37,39]. Hence, the conformation of the N terminus of Arc-NL is different in the E5 and H11 complexes.

Table 4 summarizes the interfaces of the complexes. For both Arc-nanobody complexes, there is one main interface contributing to the complex formation that is estimated to lead to a solvation free energy gain ($\Delta G_s < 0$) in an interaction-specific manner (i.e., not because of crystal packing), represented by $P < 0.5$ [56]. The crystal structures show that for both nanobodies, CDR3 is the main contributor to complex formation (Fig 4C), and both main-chain and side-chain hydrogen bonds are present. As discussed before [39], C-H. . .π interactions are conserved between different Arc-ligand complexes (Fig 4C). The interface between H11 and Arc-NL involves CDR1, 2, and 3 of H11, while binding between E5 and Arc-NL only involves CDR3 of the nanobody (Fig 4C, S1 and S2 Movies). This is intriguing, as the heat stability increase in the Arc-NL complex was higher for E5. The observation can be related to the higher number of hydrogen bonds present at the interface for E5, as well as the larger interaction area (Table 4). In both complexes, Glu^{215} of Arc forms a salt bridge to the nanobody (Fig 4C). This feature is also seen in the complex with the TARPγ2 peptide [39,41], indicating a novel recognition motif for ligand binding in Arc-NL.

According to the protein interface statistics, the formation of the Arc-NL-H11 interface appears to be slightly more favorable energetically than for Arc-NL-E5 (ΔG_s [Arc-NL-H11] < ΔG_s [Arc-NL-E5]). It should be noted that the calculated ΔG_s is based on comparison of the

Table 3. Thermal denaturation midpoints (T_m) of Arc-NL, E5, H11, and Arc-nanobody complexes Arc-NL-E5 and Arc-NL-H11. The best-fit V50 value of the Boltzmann function applied to the thermal denaturation curve is shown together with its 95 % confidence interval.

Protein	T_m (˚C)	95% CI (˚C)
Arc-NL	54.33	(53.29, 55.39)
E5	45.07	(42.72, 47.00)
H11	55.97	(54.45, 57.36)
Arc-NL-E5	61.16	(58.82, 63.93)
Arc-NL-H11	56.97	(55.10, 58.82)

https://doi.org/10.1371/journal.pone.0300453.t003

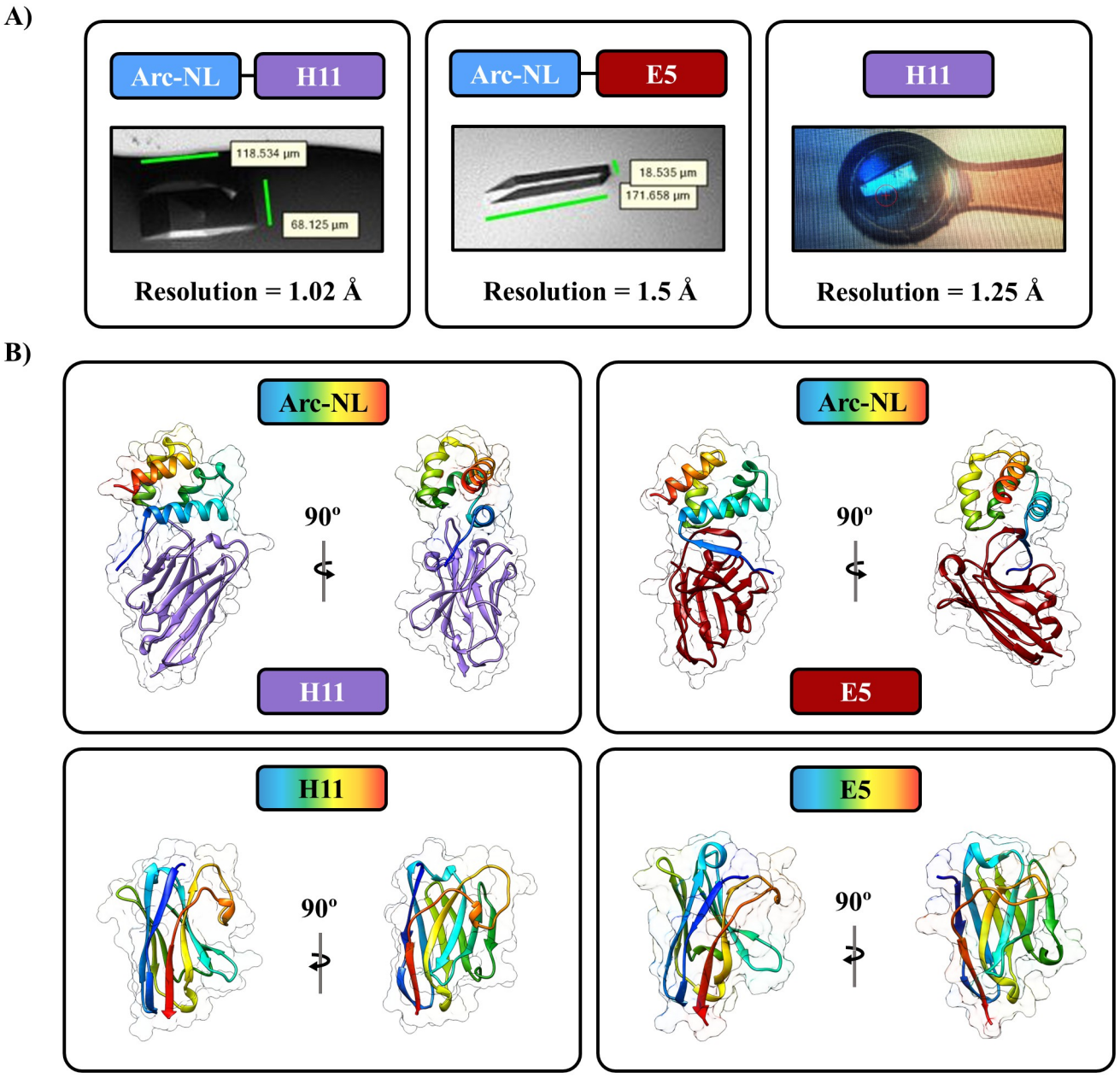

Fig 3. Protein crystals and refined structures for Arc-NL-H11, Arc-NL-E5 and H11. (A) Crystals of Arc-NL-H11, Arc-NL-E5 and unbound H11. (B) The structures of Arc-NL-H11 (top left), Arc-NL-E5 (top right) and unbound H11 (bottom left). The apo E5 structure (bottom right) was previously solved (PDB ID: 7R20) [40] and is shown for comparison with the Arc-NL-E5 complex.

https://doi.org/10.1371/journal.pone.0300453.g003

structures in complex and alone with regard to solvation free energy, and it does not include contributions from hydrogen bonds or salt bridges formed at the interface. However, the measured T_m implies that Arc-NL-E5 is more stable than Arc-NL-H11 (T_m [Arc-NL-E5] > T_m [Arc-NL-H11]). Taken together, the two nanobodies bind to overlapping epitopes on Arc-NL with unique modes of interaction, however producing similar affinity. The differences in T_m values using different methods here and before [40] indicate that while an increased T_m is a sign of binding, it does not directly correlate with binding affinity (K_D).

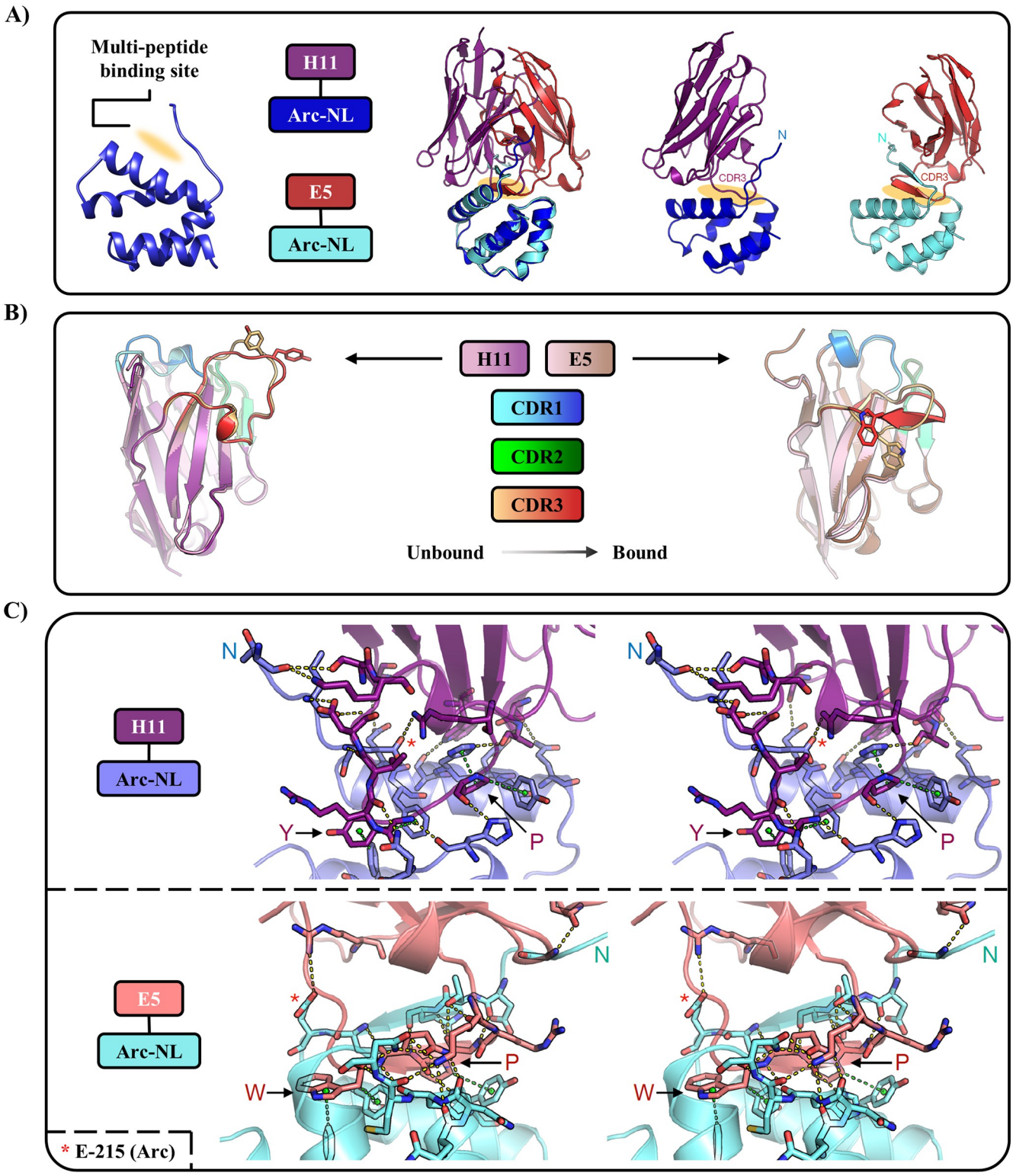

Fig 4. Structural analysis of Arc-nanobody complexes. (A) Both E5 and H11 bind to the multi-peptide binding pocket (orange shading) of Arc-NL. Left: An overlay of Arc-NL in both complexes. The Arc-NL-H11 complex (middle) and Arc-NL-E5 (right) show different conformations for the Arc-NL N terminus. (B) Overlay of bound and unbound H11 and E5, showing the conformational changes, especially in CDR3, that each nanobody displays when binding Arc-NL. The aromatic residue of the segment binding to the Arc-NL pocket is shown. (C) Intermolecular interactions between each nanobody and Arc-NL (stereo view). The CDR3 of both nanobodies is the main contributor to the protein complex formation. Top: Arc-NL bound to H11. P/Y: The PxY

motif in H11. Bottom: Arc-NL bound to E5. P/W: The PxW motif in E5. Red asterisk: Glu^{215}, which forms a salt bridge in both complexes. Interactions are shown with dashed lines: Hydrogen bonds/salt bridges in yellow and C-H. . .π interactions in green. An animated view of both complexes can be found in S1 and S2 Movies.

https://doi.org/10.1371/journal.pone.0300453.g004

The structural study of unbound E5 and H11 provides a potential explanation for the weak ellipticity found above 210 nm in CD/SRCD spectra. E5 contains Trp^{38} that is close to a disulfide bond between Cys^{24} and Cys^{97} [40]. The structure of unbound H11 also shows this feature; Trp^{38} is located next to a disulfide bond (Cys^{24}-Cys^{98}). Aromatic residues can distort the CD spectra of β-strand-containing proteins by inducing positive ellipticity around 215-225 nm [73,74], especially if they are located close to disulfide bonds [75]. Therefore, this common nanobody structural feature can explain the observed characteristic CD spectra.

Nanobodies E5 and H11 displace a TARPγ2 peptide from the Arc-NL peptide binding pocket

The thermodynamic properties of the Arc-NL-nanobody complex formation were determined using ITC. The thermodynamic parameters associated with all ITC assays are presented in Table 5. The individual replicates carried out for Arc-nanobody interactions are shown in S1 Fig. Both nanobodies show a similar profile, binding to Arc-NL with high affinity ($K_D \approx 1$ nM) in an enthalpy-driven process ($\Delta H \approx$ -23 kcal/mol) (Fig 5A). The observed unfavorable entropy can be indicative of e.g. ordering of the long CDR3 loop upon binding. Arc-NL shows exothermic binding (K_D = 5.3 μM) to a TARPγ2-derived peptide (P1), while binding is not observed when titrating the reverse control peptide (P2) (Fig 5B). The peptides used here carried a FITC label as well as a TAT sequence, and the experiment shows that P1 binds Arc-NL with an affinity similar to that observed before for a TARPγ2 peptide without tags, confirming the P1 peptide is functional and can be used in cell-based experiments. A displacement assay was carried out for both nanobodies; each assay consisted of the titration of the nanobody into a solution of Arc-NL saturated with P1 (Fig 5C and 5D, Table 5). Both nanobodies show an apparent reduction of their binding affinity and binding enthalpy. The reduction in binding enthalpy corresponds in both cases to 11-13 kcal/mol, which is close to the dissociation enthalpy of P1 and Arc-NL ($-\Delta H$ = 14.9 kcal/mol). This implies that the dissociation of P1 and Arc-NL is coupled to the association between E5/H11 and Arc-NL, suggesting that both nanobodies can displace the TARPγ2-derived peptide from Arc-NL. In addition to the crystal structures, this is supported by the fact that P1 and the CDR3s of both nanobodies contain the consensus motif for binding to Arc-NL: PxY/W/F (Fig 5E).

Table 4. Protein interface analysis of the Arc-NL-H11 and Arc-NL-E5 complexes. Main parameters derived from PISA. The main interface that contributes to the complex formation and its associated parameters are shown. The detection of two salt bridges in the H11 complex results from a double conformation of a single Arg residue at the interface.

Parameter	Arc-NL-H11 interface		Arc-NL-E5 interface	
Proteins	Arc-NL	H11	Arc-NL	E5
Area (Å^2)	1017.7		1077.4	
Residues involved (no.)	25	26	28	26
ΔG_s (kcal/mol)	-9.4		-9.1	
ΔG_s (P-value)	0.20		0.35	
Hydrogen bonds (no.)	8		14	
Salt bridges (no.)	2		1	

https://doi.org/10.1371/journal.pone.0300453.t004

Table 5. Thermodynamic parameters. For Arc-nanobody assays, four replicates were analyzed (n = 4); the mean best-fit values ± SEM of their thermodynamic binding properties are displayed. For the P1/P2-Arc-NL assays and the displacement assays, single high-quality replicates were taken. For each individual replicate, the binding affinity and enthalpy are shown alongside their 68.3% CI (± σ), as they are measures directly calculated from the experimental thermograms by SEDPHAT [67]. Abbreviations: ΔG, free energy of binding; ΔG_{App}, apparent free energy of binding; ΔH, binding enthalpy; ΔH_{App}, apparent binding enthalpy; CI, confidence interval; K_D, binding affinity (dissociation constant); $K_{D\text{-}App}$, apparent binding affinity (apparent dissociation constant); P1, FITC-labelled TARPγ2-derived peptide; P2, FITC-labelled TARPγ2 reverse peptide.

Binding assay	K_D (nM)		ΔH (kcal/mol)		-TΔS (kcal/mol)	ΔG (kcal/mol)
E5 into Arc-NL (n = 4)	0.99 ± 0.27		-23.24 ± 0.40		+10.97 ± 0.30	-12.27 ± 0.22
H11 into Arc-NL (n = 4)	1.14 ± 0.56		-23.48 ± 0.71		+11.26 ± 0.43	-12.22 ± 0.41
Binding assay	**K_D (μM)**	**K_D—68.3% CI (μM)**	**ΔH (kcal/mol)**	**ΔH—68.3% CI (kcal/mol)**	**-TΔS (kcal/mol)**	**ΔG (kcal/mol)**
P1 into Arc-NL (n = 1)	5.31	(5.02, 5.62)	-14.86	(-14.96,-14.77)	+7.79	-7.08
P2 into Arc-NL (n = 1)	$6.92 \cdot 10^{21}$	-	0.049	-	+25.22	+25.27
Displacement assay	**$K_{D\text{-}App}$ (nM)**	**$K_{D\text{-}App}$—68.3% CI (nM)**	**ΔH_{App} (kcal/mol)**	**ΔH_{App}—68.3% CI (kcal/mol)**	**$-T\Delta S_{App}$ (kcal/mol)**	**ΔG_{App} (kcal/mol)**
E5 into Arc-NL-P1 (n = 1)	6.93	(1.00, 14.69)	-11.98	(-12.20,-11.76)	+1.03	-10.95
H11 into Arc-NL-P1 (n = 1)	10.38	(2.48, 25.73)	-10.30	(-10.83,-9.81)	-0.411	-10.71

https://doi.org/10.1371/journal.pone.0300453.t005

The above experiments show that binding between TARPγ2 and Arc-NL can be inhibited by the anti-Arc nanobodies E5 and H11. The apparent thermodynamic values in the competition experiment are a combination of the complex process of peptide dissociation and nanobody binding, and they are not analyzed further here. Although displacement assays were not performed for other Arc ligands, binding to the Arc-NL peptide binding pocket should be similarly inhibited by E5 and H11 for other endogenous Arc-NL ligands. TARPγ2 stands out as the endogenous Arc-NL ligand with the highest known affinity [39]; therefore, if binding to TARPγ2 is blocked by H11 and E5, these two nanobodies will also displace lower-affinity ligands. Interestingly, the conformation of the Arc-NL N terminus bound to peptides derived from Arc endogenous ligands [39,41] is strikingly similar to that observed in the E5 complex (Fig 6). It is possible that conformational differences exist in flArc, when bound to either E5 or H11, as the N terminus of Arc-NL corresponds to the end of the flexible linker region. This may raise possibilities for conformation-specific binding or conformational modulation in the context of flArc, despite overlapping binding sites for the two nanobodies.

Simultaneous binding of anti-Arc-NL and anti-Arc-CL nanobodies to full-length Arc

Our earlier data, including crystal structures, showed that the nanobodies H11 and C11 independently bound to the Arc-NL and Arc-CL, respectively, at the same time [40]. Therefore, as H11 and E5 both bind to the same pocket in Arc-NL, we wished to confirm if this is also true for the nanobody pair E5 and C11.

As a control, we carried out analytical SEC of the Arc-CTdt construct with H11 and C11, i.e. the complex crystallized previously. As expected, the SEC peak for the Arc dimer moves when C11 and H11 are sequentially added (Fig 7A).

We purified the flArc dimeric mutant rArcFL-7A in complex with both E5 and C11, and we used the samples for low-resolution structural studies in solution using SEC-SAXS, as well as for molecular weight determination in SEC-MALS. In the purified complex, bands for both nanobodies can be detected in addition to flArc (Fig 7B), indicating ternary complex formation between the three proteins. In the SAXS and MALS experiments (Table 6, Fig 7C–7F), the dimeric state of flArc was confirmed, and the addition of either E5 or C11 caused an expected increase in MW. This increase was effectively doubled, when both nanobodies were added.

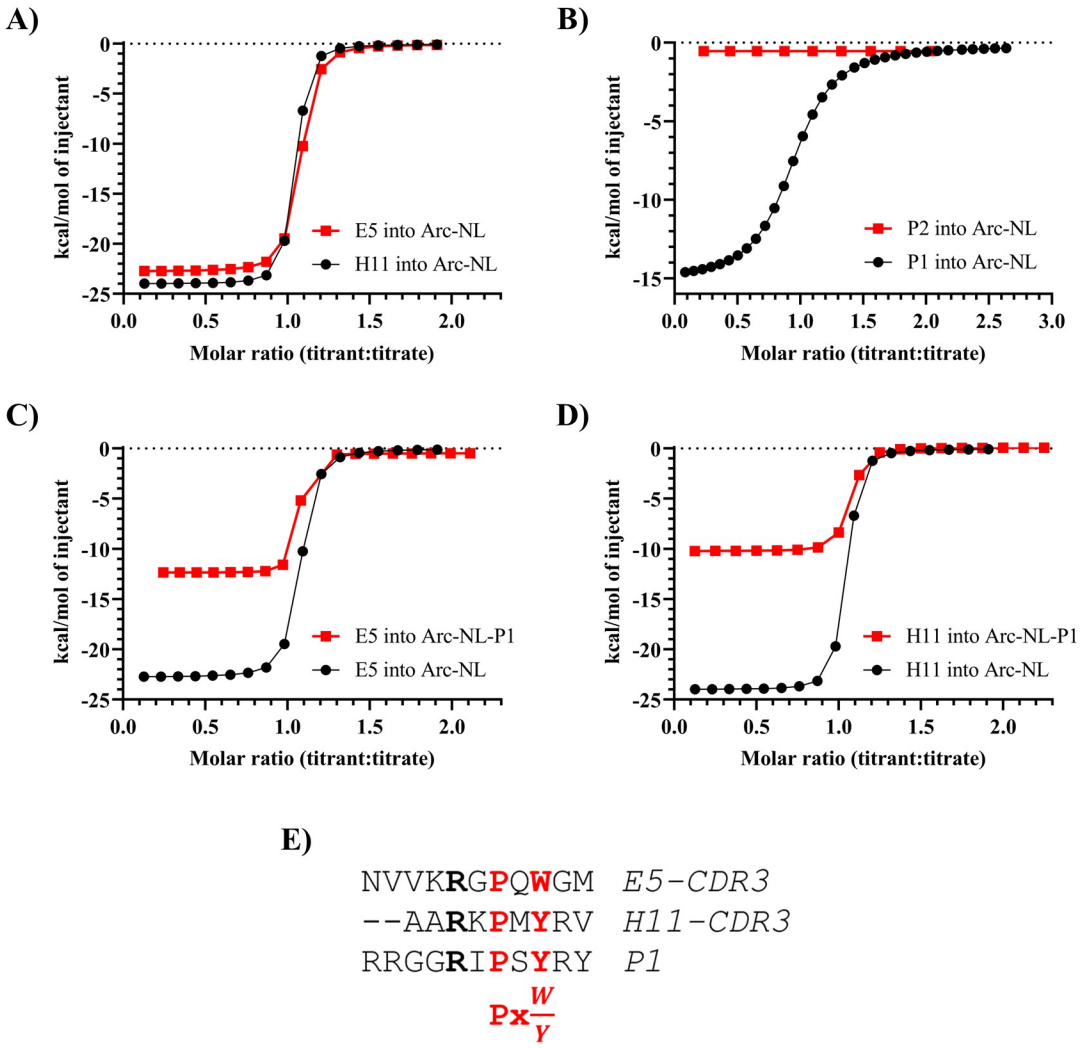

Fig 5. Thermodynamic characterization of the binding dynamics between Arc-NL, TARPγ2-derived peptides, and anti-Arc-NL nanobodies. (A) Titration of E5/H11 into Arc-NL; both nanobodies display a similar thermodynamic binding profile. Only one representative replicate of each assay is shown. (B) Titration of P1/P2 into Arc-NL; binding is selective for P1, while P2 is valid as a negative control. (C) Displacement assay for E5. An apparent reduction in K_D and ΔH can be observed. (D) Displacement assay for H11. The apparent reduction of the K_D and ΔH values is seen. (E) Multiple sequence alignment of P1 and the CDR3s of H11 and E.

https://doi.org/10.1371/journal.pone.0300453.g005

This shows simultaneous binding of both E5 and C11 to flArc, similarly to the pair H11-C11, for which we have high-resolution data from before with the Arc-CTdt [40].

SAXS was used to assess the binding sites of the nanobodies and thus, the likely location of the Arc lobe domains in the flArc dimer. The scattering curves (Fig 7D and 7E, Table 6) indicate that rArcFL7A is a dimer and that E5 and H11 can bind simultaneously in a 2:2:2 stoichiometry. Considering the current models (Fig 7F) and earlier data from complexes of Arc with nanobodies E5 and H11 (binding to the NL) and C11 (binding to the CL) [40,42], one can conclude that in the dimeric full-length Arc, the N-lobe is close to the ends of the elongated dimer, and the C-lobe is more centrally located. The dimer interface is formed by the NTD [40].

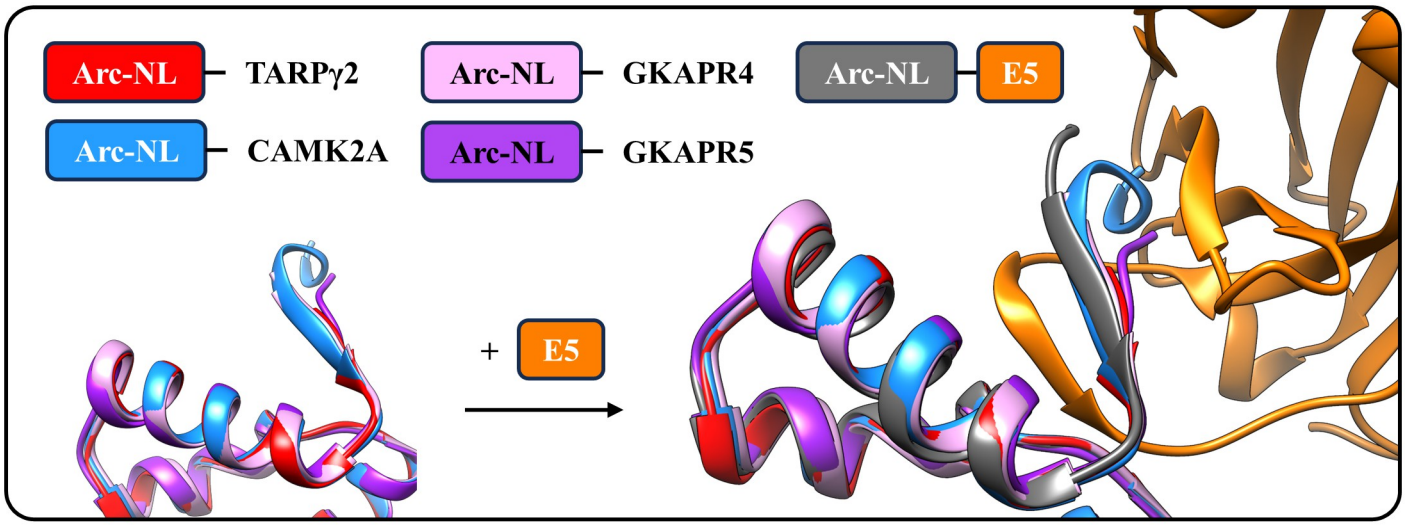

Fig 6. Comparative structural analysis of Arc-NL bound to different peptides derived from endogenous Arc ligands. The Arc N-lobe adopts a similar conformation while interacting with different ligand peptides: TARPγ2 (PDB ID: 6TNO) [39], CaMK2A (PDB ID: 4X3I) [37], GKAPR4 (PDB ID: 6TNQ) [39] and GKAPR5 (PDB ID: 6TQ0) [39]. The same conformation is present in the complex between E5 and Arc-NL.

https://doi.org/10.1371/journal.pone.0300453.g006

Insights into potential binding partners of Arc-NL

To search for potential binding partners of Arc-NL, the CDR3 sequences of both E5 and H11 were used for database searches. The search was restricted to human, mouse, and rat protein sequences. For each CDR3, an interesting match was noted (see below). Several other matches were considered, and some of them are collected in S1 Table. Such a short sequence gives many hits, especially if one looks at the Arc-NL binding motif alone.

For the E5 CDR3, all selected hits show the consensus motif PxW (S2 Fig); note that E5 is the only currently known ligand of Arc-NL with a Trp residue in the aromatic position. Therefore, it would be interesting to find possible endogenous ligands with the same motif. The closest hit was cathepsin H. Cathepsins are proteases targeted to endosomes and lysosomes, with roles in regulation of lysosomal dynamics and autophagy. Current evidence implicates neuronal activity-dependent regulation of lysosomes and autophagy in synaptic plasticity and memory formation [76–79]. Activity-dependent interaction between cathepsin H and Arc could be tested as a hypothesis.

Among the short-listed hits for the H11 CDR3, only the PRKCA-binding protein displays the PxY consensus motif (S2 Fig); the sequence corresponds to the protein PICK1 [80]. PICK1 is involved in the endocytosis of AMPAR and interacts directly with Arc through its BAR domain (amino acids 152-362) [81,82]. Fig 8 shows homology between the H11 CDR3 and PICK1 amino acids 278-294 in the BAR domain; this segment corresponds to a flexible loop at the end of the BAR domain and would therefore be well accessible for Arc-NL binding. Thus, the H11 nanobody CDR3 loop may have helped in identifying the specific Arc interaction site on PICK1. This hypothesis can be tested in further experiments to reveal molecular details of the Arc-PICK1 interaction.

Conclusions

Nanobodies are emerging as versatile molecular tools for both basic and translational research. We characterized the structural and functional properties of two nanobodies (H11 and E5)

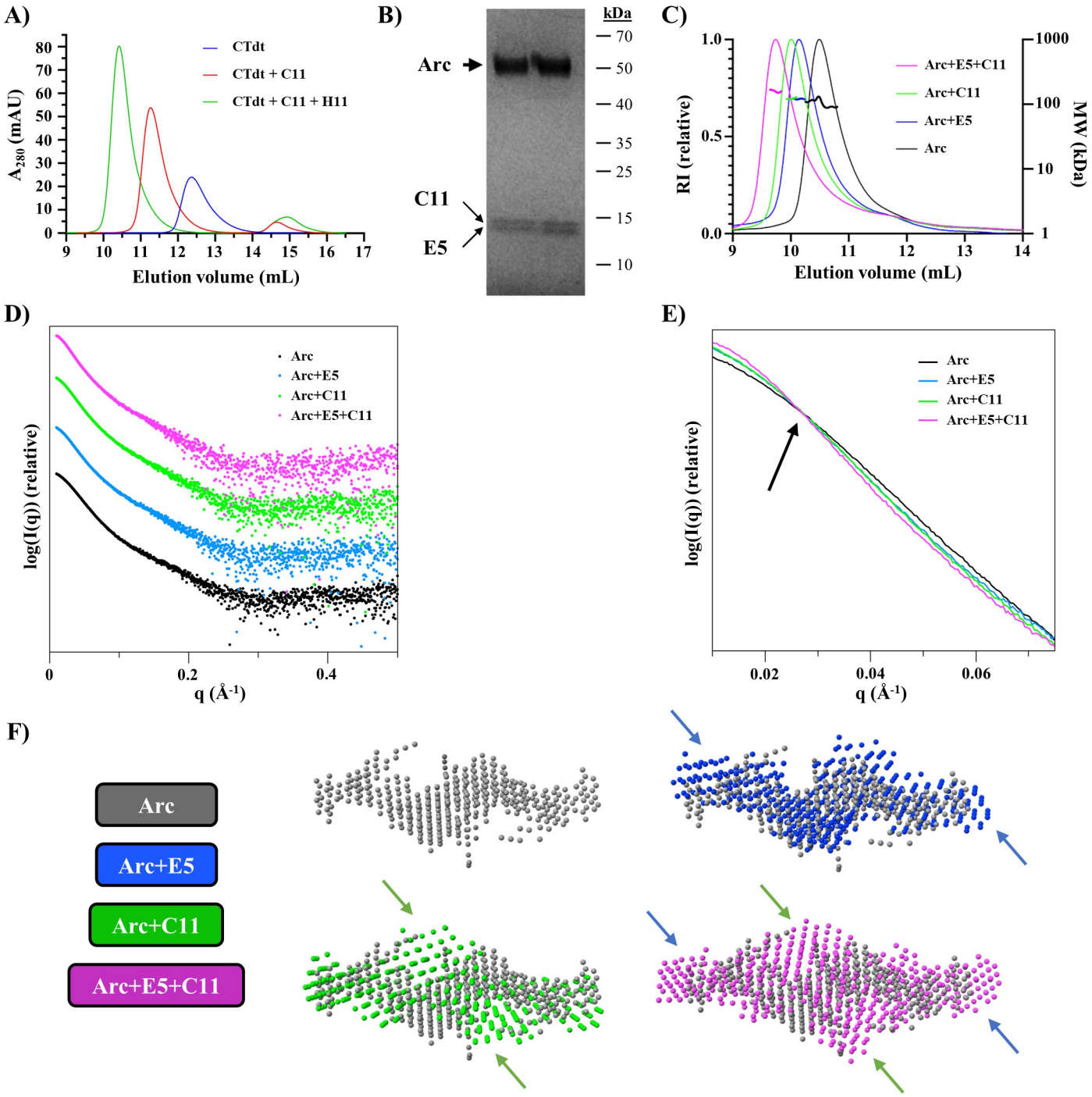

Fig 7. Binding of two nanobodies simultaneously. (A) Analytical SEC of Arc-CTdt with nanobodies C11 and H11 indicates simultaneous binding. (B) SDS-PAGE of purified ternary complex rArcFL-7A+E5+C11. Arc is shown with the thick arrow and the two nanobodies with thin arrows. (C) SEC-MALS of rArcFL-7A with nanobodies E5 and C11. (D) SAXS data; displaced along the y axis for clarity. (E) Zoom-in of the low-angle region indicates different shapes for the scattering curves, with an increase in size upon addition of each nanobody. The crossover point is indicated by an arrow. The SAXS curves were scaled together for the analysis. (F) Ab initio dummy atom models for Arc (gray), Arc+E5 (blue), Arc+C11 (green), Arc+E5+C11 (magenta). Apparent positions of extra density upon nanobody addition are shown with arrows.

https://doi.org/10.1371/journal.pone.0300453.g007

Table 6. SAXS and SEC-MALS parameters. All data point towards the binding of E5 and H11 to the Arc dimer simultaneously, resulting in a 2:2:2 ternary complex.

Complex	*rArcFL7A*	*+E5*	*+C11*	*+E5 and C11*
Oligomeric state/ stoichiometry	Dimer	2:2	2:2	2:2:2
Theoretical mass (kDa)	90.0	115.6	116.2	141.7
Mass from SEC-MALS (kDa)	104.9	122.0	123.4	163.0
Mass from SAXS Bayesian estimate (kDa)	109.1	130.1	138.2	157.1
Guinier R_g (Å)	47.4	55.8	57.2	59.8
P(r) R_g (Å)	50.5	58.5	56.6	63.7
D_{max} (Å)	200	228	211	236
Porod volume (nm^3)	230	298	294	350

https://doi.org/10.1371/journal.pone.0300453.t006

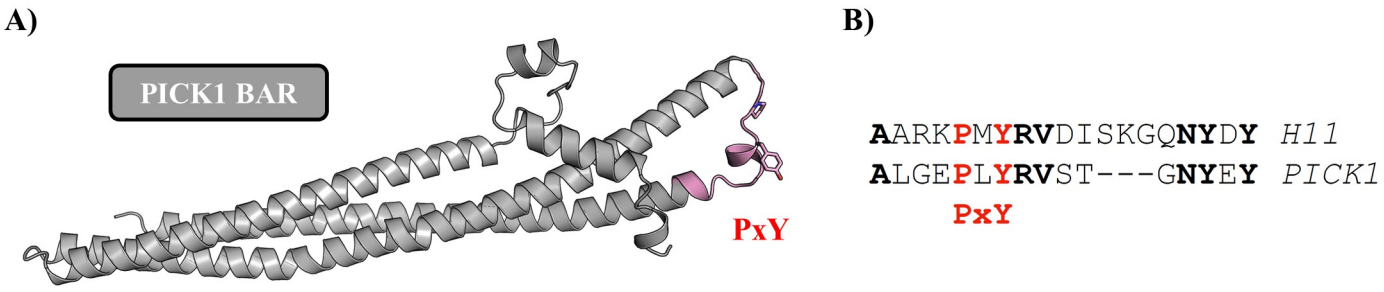

Fig 8. Identification of a putative Arc-NL binding site on PICK1. (A) AlphaFold2 model of the PICK1 BAR domain shows that the distal loop carries a PxY motif (pink). The side chains of the Pro and Tyr residues in the motif are shown. (B) Sequence alignment between the H11 CDR3 loop and the PxY motif of PICK1. Bold residues are identical, and the PxY motif is highlighted in red.

https://doi.org/10.1371/journal.pone.0300453.g008

against Arc, a complex molecular regulator of synaptic plasticity. Our results pave the way towards the use of anti-Arc nanobodies H11 and E5 as molecular modulators of Arc *in vitro* and *in vivo*, possibly in combination with nanobodies simultaneously targeting the Arc-CL. Structural biology of different oligomeric forms of Arc will benefit from the use of different nanobody combinations. Besides, genetically encoded nanobodies can be expressed in living cells to manipulate target protein function or label proteins for super-resolution microscopy, highlighting nanobodies as diagnostic and functional tools [83,84]. Furthermore, several strategies are being developed to promote the use of nanobodies in the treatment and diagnosis of brain diseases *in vivo* [85–87]. For example, nanobodies have been successfully used to treat an animal model of Alzheimer's disease [88]. Considering the latest advances in nanobody-associated research, the use of anti-Arc nanobodies for behavioral, diagnostic, and therapeutic purposes is within range of current translational neuroscience. Anti-Arc nanobodies E5 and H11 provide molecular tools to selectively study how Arc structure, function, and oligomerization influence memory, learning, stress regulation, and neuropathologies.

Supporting information

S1 Fig. ITC assays for Arc-nanobody interactions (individual replicates).
(TIF)

S2 Fig. Sequence alignments between CDR3 sequences and the top hits.
(PDF)

S1 Table. Top hits from the nanobody CDR3 BLAST search.
(PDF)

S1 Movie. Animation of the complex between Arc-NL and nanobody H11.
(MPG)

S2 Movie. Animation of the complex between Arc-NL and nanobody E5.
(MPG)

Acknowledgments

We are grateful to Ju Xu and Anne Baumann for technical assistance during this study, and we acknowledge the use of the Core Facility for Biophysics, Structural Biology, and Screening (BiSS) at the University of Bergen. We thank DESY (Hamburg, Germany) for the provision of their experimental facilities; part of this research was carried out on the PETRA III storage ring. Our gratitude extends to the ISA facility (Aarhus, Denmark), as part of this research was conducted on the storage ring ASTRID2. We further recognize access to and support at the SOLEIL and MAX-IV synchrotrons.

Author Contributions

Conceptualization: José M. Godoy Muñoz, Andrea J. Lopez, Clive R. Bramham, Petri Kursula.

Data curation: Lasse Neset, Sigurbjörn Markússon, Petri Kursula.

Formal analysis: José M. Godoy Muñoz, Sigurbjörn Markússon.

Investigation: José M. Godoy Muñoz, Lasse Neset, Sigurbjörn Markússon, Sarah Weber, Oda C. Krokengen, Aleksi Sutinen, Eleni Christakou, Andrea J. Lopez, Petri Kursula.

Methodology: José M. Godoy Muñoz, Sigurbjörn Markússon, Sarah Weber, Oda C. Krokengen, Aleksi Sutinen, Eleni Christakou, Andrea J. Lopez.

Project administration: Clive R. Bramham, Petri Kursula.

Resources: Clive R. Bramham.

Supervision: Andrea J. Lopez, Clive R. Bramham, Petri Kursula.

Validation: José M. Godoy Muñoz, Lasse Neset, Sigurbjörn Markússon, Petri Kursula.

Visualization: José M. Godoy Muñoz, Sigurbjörn Markússon.

Writing – original draft: José M. Godoy Muñoz.

Writing – review & editing: Lasse Neset, Sigurbjörn Markússon, Clive R. Bramham, Petri Kursula.

References

1. Brod G, Werkle-Bergner M, Shing YL. The Influence of Prior Knowledge on Memory: A Developmental Cognitive Neuroscience Perspective. Front Behav Neurosci. 2013; 7. https://doi.org/10.3389/fnbeh.2013.00139 PMID: 24115923
2. Martin SJ, Grimwood PD, Morris RGM. Synaptic Plasticity and Memory: An Evaluation of the Hypothesis. Annu Rev Neurosci. 2000; 23: 649–711. https://doi.org/10.1146/annurev.neuro.23.1.649 PMID: 10845078

3. Takeuchi T, Duszkiewicz AJ, Morris RGM. The synaptic plasticity and memory hypothesis: encoding, storage and persistence. Philos Trans R Soc B: Biol Sci. 2014; 369: 20130288. https://doi.org/10.1098/rstb.2013.0288 PMID: 24298167

4. Abraham WC, Jones OD, Glanzman DL. Is plasticity of synapses the mechanism of long-term memory storage? NPJ Sci Learn. 2019; 4: 9. https://doi.org/10.1038/s41539-019-0048-y PMID: 31285847

5. Lu J, Zuo Y. Shedding light on learning and memory: optical interrogation of the synaptic circuitry. Curr Opin Neurobiol. 2021; 67: 138–144. https://doi.org/10.1016/j.conb.2020.10.015 PMID: 33279804

6. Citri A, Malenka RC. Synaptic plasticity: Multiple forms, functions, and mechanisms. Neuropsychopharmacology. 2008; 33: 18–41. https://doi.org/10.1038/sj.npp.1301559 PMID: 17728696

7. Vazdarjanova A, Ramirez-Amaya V, Insel N, Plummer TK, Rosi S, Chowdhury S, et al. Spatial exploration induces ARC, a plasticity-related immediate-early gene, only in calcium/calmodulin-dependent protein kinase II-positive principal excitatory and inhibitory neurons of the rat forebrain. J Comp Neurol. 2006; 498: 317–329. https://doi.org/10.1002/cne.21003 PMID: 16871537

8. Bramham CR, Alme MN, Bittins M, Kuipers SD, Nair RR, Pai B, et al. The Arc of synaptic memory. Exp Brain Res. 2010; 200: 125–140. https://doi.org/10.1007/s00221-009-1959-2 PMID: 19690847

9. Link W, Konietzko U, Kauselmann G, Krug M, Schwanke B, Frey U, et al. Somatodendritic expression of an immediate early gene is regulated by synaptic activity. Proc Natl Acad Sci USA. 1995; 92: 5734–5738. https://doi.org/10.1073/pnas.92.12.5734 PMID: 7777577

10. Lyford GL, Yamagata K, Kaufmann WE, Barnes CA, Sanders LK, Copeland NG, et al. Arc, a growth factor and activity-regulated gene, encodes a novel cytoskeleton-associated protein that is enriched in neuronal dendrites. Neuron. 1995; 14: 433–445. https://doi.org/10.1016/0896-6273(95)90299-6 PMID: 7857651

11. Guzowski JF, Lyford GL, Stevenson GD, Houston FP, McGaugh JL, Worley PF, et al. Inhibition of activity-dependent arc protein expression in the rat hippocampus impairs the maintenance of long-term potentiation and the consolidation of long-term memory. J Neurosci. 2000; 20: 3993–4001. https://doi.org/10.1523/JNEUROSCI.20-11-03993.2000 PMID: 10818134

12. Ploski JE, Pierre VJ, Smucny J, Park K, Monsey MS, Overeem KA, et al. The activity-regulated cytoskeletal-associated protein (Arc/Arg3.1) is required for memory consolidation of pavlovian fear conditioning in the lateral amygdala. J Neurosci. 2008; 28: 12383–12395. https://doi.org/10.1523/JNEUROSCI.1662-08.2008 PMID: 19020031

13. Holloway CM, McIntyre CK. Post-training disruption of Arc protein expression in the anterior cingulate cortex impairs long-term memory for inhibitory avoidance training. Neurobiol Learn Mem. 2011; 95: 425–432. https://doi.org/10.1016/j.nlm.2011.02.002 PMID: 21315825

14. Ons S, Martí O, Armario A. Stress-induced activation of the immediate early gene Arc (activity-regulated cytoskeleton-associated protein) is restricted to telencephalic areas in the rat brain: Relationship to c-fos mRNA. J Neurochem. 2004; 89: 1111–1118. https://doi.org/10.1111/j.1471-4159.2004.02396.x PMID: 15147503

15. Penrod RD, Kumar J, Smith LN, McCalley D, Nentwig TB, Hughes BW, et al. Activity-regulated cytoskeleton-associated protein (Arc/Arg3.1) regulates anxiety- and novelty-related behaviors. Genes Brain Behav. 2019; 18: 678–687. https://doi.org/10.1111/gbb.12561 PMID: 30761730

16. Soulé J, Alme M, Myrum C, Schubert M, Kanhema T, Bramham CR. Balancing arc synthesis, mRNA decay, and proteasomal degradation: Maximal protein expression triggered by rapid eye movement sleep-like bursts of muscarinic cholinergic receptor stimulation. J Biol Chem. 2012; 287: 22354–22366. https://doi.org/10.1074/jbc.M112.376491 PMID: 22584581

17. Thompson CL, Wisor JP, Lee CK, Pathak SD, Gerashchenko D, Smith KA, et al. Molecular and anatomical signatures of sleep deprivation in the mouse brain. Front Neurosci. 2010; 4: 1–20. https://doi.org/10.3389/fnins.2010.00165 PMID: 21088695

18. Palop JJ, Chin J, Bien-Ly N, Massaro C, Yeung BZ, Yu G-QQ, et al. Vulnerability of dentate granule cells to disruption of Arc expression in human amyloid precursor protein transgenic mice. J Neurosci. 2005; 25: 9686–9693. https://doi.org/10.1523/JNEUROSCI.2829-05.2005 PMID: 16237173

19. Wang DC, Chen SS, Lee YC, Chen TJ. Amyloid-β at sublethal level impairs BDNF-induced arc expression in cortical neurons. Neurosci Lett. 2006; 398: 78–82. https://doi.org/10.1016/j.neulet.2005.12.057 PMID: 16412575

20. Palop JJ, Chin J, Roberson ED, Wang J, Thwin MT, Bien-Ly N, et al. Aberrant Excitatory Neuronal Activity and Compensatory Remodeling of Inhibitory Hippocampal Circuits in Mouse Models of Alzheimer's Disease. Neuron. 2007; 55: 697–711. https://doi.org/10.1016/j.neuron.2007.07.025 PMID: 17785178

21. Kerrigan TL, Randall AD. A new player in the "synaptopathy" of Alzheimer's disease—Arc/Arg 3.1. Front Neurol. 2013; 4 FEB: 1–7. https://doi.org/10.3389/fneur.2013.00009 PMID: 23407382

22. Landgren S, Von Otter M, Palmér MS, Zetterström C, Nilsson S, Skoog I, et al. A novel ARC gene polymorphism is associated with reduced risk of Alzheimer's disease. J Neural Transm. 2012; 119: 833–842. https://doi.org/10.1007/s00702-012-0823-x PMID: 22622366

23. Korb E, Finkbeiner S. Arc in synaptic plasticity: from gene to behavior. Trends Neurosci. 2011; 34: 591–598. https://doi.org/10.1016/j.tins.2011.08.007 PMID: 21963089

24. Toro R, Konyukh M, Delorme R, Leblond C, Chaste P, Fauchereau F, et al. Key role for gene dosage and synaptic homeostasis in autism spectrum disorders. Trends Genet. 2010; 26: 363–372. https://doi.org/10.1016/j.tig.2010.05.007 PMID: 20609491

25. Epstein I, Finkbeiner S. The Arc of cognition: Signaling cascades regulating Arc and implications for cognitive function and disease. Semin Cell Dev Biol. 2018; 77: 63–72. https://doi.org/10.1016/j.semcdb.2017.09.023 PMID: 29559111

26. Chowdhury S, Shepherd JD, Okuno H, Lyford G, Petralia RS, Plath N, et al. Arc/Arg3.1 Interacts with the Endocytic Machinery to Regulate AMPA Receptor Trafficking. Neuron. 2006; 52: 445–459. https://doi.org/10.1016/j.neuron.2006.08.033 PMID: 17088211

27. Shepherd JD, Rumbaugh G, Wu J, Chowdhury S, Plath N, Kuhl D, et al. Arc/Arg3.1 Mediates Homeostatic Synaptic Scaling of AMPA Receptors. Neuron. 2006; 52: 475–484. https://doi.org/10.1016/j.neuron.2006.08.034 PMID: 17088213

28. Messaoudi E, Kanhema T, Soulé J, Tiron A, Dagyte G, da Silva B, et al. Sustained Arc/Arg3.1 Synthesis Controls Long-Term Potentiation Consolidation through Regulation of Local Actin Polymerization in the Dentate Gyrus In Vivo. J Neurosci. 2007; 27: 10445–10455. https://doi.org/10.1523/JNEUROSCI.2883-07.2007 PMID: 17898216

29. Korb E, Wilkinson CL, Delgado RN, Lovero KL, Finkbeiner S. Arc in the nucleus regulates PML-dependent GluA1 transcription and homeostatic plasticity. Nat Neurosci. 2013; 16: 874–883. https://doi.org/10.1038/nn.3429 PMID: 23749147

30. Leung H-W, Foo G, VanDongen A. Arc Regulates Transcription of Genes for Plasticity, Excitability and Alzheimer's Disease. Biomedicines. 2022; 10: 1946. https://doi.org/10.3390/biomedicines10081946 PMID: 36009494

31. Mergiya TF, Gundersen JET, Kanhema T, Brighter G, Ishizuka Y, Bramham CR. Detection of Arc/Arg3.1 oligomers in rat brain: constitutive and synaptic activity-evoked dimer expression in vivo. Front Mol Neurosci. 2023; 16. https://doi.org/10.3389/fnmol.2023.1142361 PMID: 37363319

32. Eriksen MS, Bramham CR. Molecular physiology of Arc/Arg3.1: The oligomeric state hypothesis of synaptic plasticity. Acta Physiol. 2022; 236: e13886. https://doi.org/10.1111/apha.13886 PMID: 36073248

33. Zhang W, Chuang YA, Na Y, Ye Z, Yang L, Lin R, et al. Arc Oligomerization Is Regulated by CaMKII Phosphorylation of the GAG Domain: An Essential Mechanism for Plasticity and Memory Formation. Mol Cell. 2019; 75: 13–25.e5. https://doi.org/10.1016/j.molcel.2019.05.004 PMID: 31151856

34. Hallin EI, Eriksen MS, Baryshnikov S, Nikolaienko O, Grødem S, Hosokawa T, et al. Structure of monomeric full-length ARC sheds light on molecular flexibility, protein interactions, and functional modalities. J Neurochem. 2018; 147. https://doi.org/10.1111/jnc.14556 PMID: 30028513

35. Myrum C, Baumann A, Bustad HJ, Flydal MI, Mariaule V, Alvira S, et al. Arc is a flexible modular protein capable of reversible self-oligomerization. Biochem J. 2015; 468: 145–158. https://doi.org/10.1042/BJ20141446 PMID: 25748042

36. Pastuzyn ED, Day CE, Kearns RB, Kyrke-Smith M, Taibi A V., McCormick J, et al. The Neuronal Gene Arc Encodes a Repurposed Retrotransposon Gag Protein that Mediates Intercellular RNA Transfer. Cell. 2018; 172: 275–288.e18. https://doi.org/10.1016/j.cell.2017.12.024 PMID: 29328916

37. Zhang W, Wu J, Ward MD, Yang S, Chuang Y, Xiao M, et al. Structural Basis of Arc Binding to Synaptic Proteins: Implications for Cognitive Disease. Neuron. 2015; 86: 490–500. https://doi.org/10.1016/j.neuron.2015.03.030 PMID: 25864631

38. Eriksen MS, Nikolaienko O, Hallin EI, Grødem S, Bustad HJ, Flydal MI, et al. Arc self-association and formation of virus-like capsids are mediated by an N-terminal helical coil motif. FEBS J. 2021; 288: 2930–2955. https://doi.org/10.1111/febs.15618 PMID: 33175445

39. Hallin EI, Bramham CR, Kursula P. Structural properties and peptide ligand binding of the capsid homology domains of human Arc. Biochem Biophys Rep. 2021; 26: 100975. https://doi.org/10.1016/j.bbrep.2021.100975 PMID: 33732907

40. Markússon S, Hallin EI, Bustad HJ, Raasakka A, Xu J, Muruganandam G, et al. High-affinity anti-Arc nanobodies provide tools for structural and functional studies. PLoS One. 2022; 17: e0269281. https://doi.org/10.1371/journal.pone.0269281 PMID: 35671319

41. Zhang W, Wu J, Ward MD, Yang S, Chuang Y, Xiao M, et al. Structural basis of arc binding to synaptic proteins: implications for cognitive disease. Neuron. 2015; 86: 490–500. https://doi.org/10.1016/j.neuron.2015.03.030 PMID: 25864631

42. Ishizuka Y, Mergiya TF, Baldinotti R, Xu J, Hallin EI, Markússon S, et al. Development and Validation of Arc Nanobodies: New Tools for Probing Arc Dynamics and Function. Neurochem Res. 2022; 47: 2656–2666. https://doi.org/10.1007/s11064-022-03573-5 PMID: 35307777

43. Busso D, Delagoutte-Busso B, Moras D. Construction of a set Gateway-based destination vectors for high-throughput cloning and expression screening in Escherichia coli. Anal Biochem. 2005; 343: 313–321. https://doi.org/10.1016/j.ab.2005.05.015 PMID: 15993367

44. Hammarström M, Woestenenk EA, Hellgren N, Härd T, Berglund H. Effect of N-terminal solubility enhancing fusion proteins on yield of purified target protein. J Struct Funct Genomics. 2006; 7: 1–14. https://doi.org/10.1007/s10969-005-9003-7 PMID: 16850178

45. Miles AJ, Wallace BA. CDtoolX, a downloadable software package for processing and analyses of circular dichroism spectroscopic data. Protein Sci. 2018; 27: 1717–1722. https://doi.org/10.1002/pro.3474 PMID: 30168221

46. Greenfield NJ. Using circular dichroism collected as a function of temperature to determine the thermodynamics of protein unfolding and binding interactions. Nat Protoc. 2006; 1: 2527–2535. https://doi.org/10.1038/nprot.2006.204 PMID: 17406506

47. Micsonai A, Wien F, Kernya L, Lee Y-H, Goto Y, Réfrégiers M, et al. Accurate secondary structure prediction and fold recognition for circular dichroism spectroscopy. Proc Natl Acad Sci USA. 2015; 112. https://doi.org/10.1073/pnas.1500851112 PMID: 26038575

48. Khrapunov S. Circular dichroism spectroscopy has intrinsic limitations for protein secondary structure analysis. Anal Biochem. 2009; 389: 174–176. https://doi.org/10.1016/j.ab.2009.03.036 PMID: 19332020

49. Nagy G, Grubmüller H. How accurate is circular dichroism-based model validation? Eur Biophys J. 2020; 49: 497–510. https://doi.org/10.1007/s00249-020-01457-6 PMID: 32844286

50. Burkhardt A, Pakendorf T, Reime B, Meyer J, Fischer P, Stübe N, et al. Status of the crystallography beamlines at PETRA III. Eur Phys J Plus. 2016; 131: 56. https://doi.org/10.1140/epjp/i2016-16056-0

51. Kabsch W. XDS. Acta Crystallogr D Biol Crystallogr. 2010; 66: 125–132. https://doi.org/10.1107/S0907444909047337 PMID: 20124692

52. Zwart PH, Grosse-Kunstleve RW, Adams PD. Xtriage and Fest: automatic assessment of X-ray data and substructure structure factor estimation. CCP4 Newsletter 42. 2005.

53. Afonine P V., Grosse-Kunstleve RW, Echols N, Headd JJ, Moriarty NW, Mustyakimov M, et al. Towards automated crystallographic structure refinement with phenix.refine. Acta Crystallogr D Biol Crystallogr. 2012; 68: 352–367. https://doi.org/10.1107/S0907444912001308 PMID: 22505256

54. Emsley P, Lohkamp B, Scott WG, Cowtan K. Features and development of Coot. Acta Crystallogr D Biol Crystallogr. 2010; 66: 486–501. https://doi.org/10.1107/S0907444910007493 PMID: 20383002

55. Williams CJ, Headd JJ, Moriarty NW, Prisant MG, Videau LL, Deis LN, et al. MolProbity: More and better reference data for improved all-atom structure validation. Protein Sci. 2018; 27: 293–315. https://doi.org/10.1002/pro.3330 PMID: 29067766

56. Krissinel E, Henrick K. Inference of Macromolecular Assemblies from Crystalline State. J Mol Biol. 2007; 372: 774–797. https://doi.org/10.1016/j.jmb.2007.05.022 PMID: 17681537

57. Pettersen EF, Goddard TD, Huang CC, Couch GS, Greenblatt DM, Meng EC, et al. UCSF Chimera—A visualization system for exploratory research and analysis. J Comput Chem. 2004; 25: 1605–1612. https://doi.org/10.1002/jcc.20084 PMID: 15264254

58. Kahnt M, Klementiev K, Haghighat V, Weninger C, Plivelic TS, Terry AE, et al. Measurement of the coherent beam properties at the CoSAXS beamline. J Synchrotron Radiat. 2021; 28: 1948–1953. https://doi.org/10.1107/S1600577521009140 PMID: 34738950

59. Bizien T, Durand D, Roblina P, Thureau A, Vachette P, Pérez J. A Brief Survey of State-of-the-Art BioSAXS. Protein Pept Lett. 2016; 23: 217–231. https://doi.org/10.2174/0929866523666160106153655 PMID: 26732245

60. Panjkovich A, Svergun DI. CHROMIXS: automatic and interactive analysis of chromatography-coupled small-angle X-ray scattering data. Bioinformatics. 2018; 34: 1944–1946. https://doi.org/10.1093/bioinformatics/btx846 PMID: 29300836

61. Manalastas-Cantos K, Konarev P V., Hajizadeh NR, Kikhney AG, Petoukhov M V., Molodenskiy DS, et al. ATSAS 3.0: expanded functionality and new tools for small-angle scattering data analysis. J Appl Crystallogr. 2021; 54: 343–355. https://doi.org/10.1107/S1600576720013412 PMID: 33833657

62. Svergun DI. Determination of the regularization parameter in indirect-transform methods using perceptual criteria. J Appl Crystallogr. 1992; 25: 495–503. https://doi.org/10.1107/S0021889892001663

63. Svergun DI. Restoring Low Resolution Structure of Biological Macromolecules from Solution Scattering Using Simulated Annealing. Biophys J. 1999; 76: 2879–2886. https://doi.org/10.1016/S0006-3495(99)77443-6 PMID: 10354416

64. Svergun DI, Petoukhov M V., Koch MHJ. Determination of Domain Structure of Proteins from X-Ray Solution Scattering. Biophys J. 2001; 80: 2946–2953. https://doi.org/10.1016/S0006-3495(01)76260-1 PMID: 11371467

65. Brautigam CA, Zhao H, Vargas C, Keller S, Schuck P. Integration and global analysis of isothermal titration calorimetry data for studying macromolecular interactions. Nat Protoc. 2016; 11: 882–894. https://doi.org/10.1038/nprot.2016.044 PMID: 27055097

66. Scheuermann TH, Brautigam CA. High-precision, automated integration of multiple isothermal titration calorimetric thermograms: New features of NITPIC. Methods. 2015; 76: 87–98. https://doi.org/10.1016/j.ymeth.2014.11.024 PMID: 25524420

67. Zhao H, Piszczek G, Schuck P. SEDPHAT—A platform for global ITC analysis and global multi-method analysis of molecular interactions. Methods. 2015; 76: 137–148. https://doi.org/10.1016/j.ymeth.2014.11.012 PMID: 25477226

68. Brautigam CA. Calculations and Publication-Quality Illustrations for Analytical Ultracentrifugation Data. Methods Enzymol. 2015; 562: 109–133. https://doi.org/10.1016/bs.mie.2015.05.001 PMID: 26412649

69. Altschul SF, Gish W, Miller W, Myers EW, Lipman DJ. Basic local alignment search tool. J Mol Biol. 1990; 215: 403–410. https://doi.org/10.1016/S0022-2836(05)80360-2 PMID: 2231712

70. McWilliam H, Li W, Uludag M, Squizzato S, Park YM, Buso N, et al. Analysis Tool Web Services from the EMBL-EBI. Nucleic Acids Res. 2013; 41: W597–W600. https://doi.org/10.1093/nar/gkt376 PMID: 23671338

71. Waterhouse AM, Procter JB, Martin DMA, Clamp M, Barton GJ. Jalview Version 2—a multiple sequence alignment editor and analysis workbench. Bioinformatics. 2009; 25: 1189–1191. https://doi.org/10.1093/bioinformatics/btp033 PMID: 19151095

72. Greenfield NJ. Using circular dichroism spectra to estimate protein secondary structure. Nat Protoc. 2006; 1: 2876–2890. https://doi.org/10.1038/nprot.2006.202 PMID: 17406547

73. Amdursky N, Stevens MM. Circular Dichroism of Amino Acids: Following the Structural Formation of Phenylalanine. ChemPhysChem. 2015; 16: 2768–2774. https://doi.org/10.1002/cphc.201500260 PMID: 26260223

74. Andersson D, Carlsson U, Freskgård P-O. Contribution of tryptophan residues to the CD spectrum of the extracellular domain of human tissue factor. Eur J Biochem. 2001; 268: 1118–1128. https://doi.org/10.1046/j.1432-1327.2001.01981.x PMID: 11179978

75. Venyaminov SY, Yang JT. Determination of Protein Secondary Structure. In: Fasman GD, editor. Circular Dichroism and the Conformational Analysis of Biomolecules. Boston, MA: Springer US; 1996. pp. 69–107. https://doi.org/10.1007/978-1-4757-2508-7_3

76. Tran A, Silver J. Cathepsins in neuronal plasticity. Neural Regen Res. 2021; 16: 26. https://doi.org/10.4103/1673-5374.286948 PMID: 32788444

77. Kononenko NL. Lysosomes convene to keep the synapse clean. J Cell Biol. 2017; 216: 2251–2253. https://doi.org/10.1083/jcb.201707070 PMID: 28724526

78. Padamsey Z, McGuinness L, Bardo SJ, Reinhart M, Tong R, Hedegaard A, et al. Activity-Dependent Exocytosis of Lysosomes Regulates the Structural Plasticity of Dendritic Spines. Neuron. 2017; 93: 132–146. https://doi.org/10.1016/j.neuron.2016.11.013 PMID: 27989455

79. Pandey K, Yu XW, Steinmetz A, Alberini CM. Autophagy coupled to translation is required for long-term memory. Autophagy. 2021; 17: 1614–1635. https://doi.org/10.1080/15548627.2020.1775393 PMID: 32501746

80. Staudinger J, Zhou J, Burgess R, Elledge SJ, Olson EN. PICK1: a perinuclear binding protein and substrate for protein kinase C isolated by the yeast two-hybrid system. J Cell Biol. 1995; 128: 263–271. https://doi.org/10.1083/jcb.128.3.263 PMID: 7844141

81. Goo BMSS, Sanstrum BJ, Holden DZY, Yu Y, James NG. Arc/Arg3.1 has an activity-regulated interaction with PICK1 that results in altered spatial dynamics. Sci Rep. 2018; 8: 14675. https://doi.org/10.1038/s41598-018-32821-4 PMID: 30279480

82. Lorgen J-Ø, Egbenya DL, Hammer J, Davanger S. PICK1 facilitates lasting reduction in GluA2 concentration in the hippocampus during chronic epilepsy. Epilepsy Res. 2017; 137: 25–32. https://doi.org/10.1016/j.eplepsyres.2017.08.012 PMID: 28888867

83. Herce HD, Schumacher D, Schneider AFL, Ludwig AK, Mann FA, Fillies M, et al. Cell-permeable nanobodies for targeted immunolabelling and antigen manipulation in living cells. Nat Chem. 2017; 9: 762–771. https://doi.org/10.1038/nchem.2811 PMID: 28754949

84. Schneider AFL, Benz LS, Lehmann M, Hackenberger CPR. Cell-Permeable Nanobodies Allow Dual-Color Super-Resolution Microscopy in Untransfected Living Cells. Angew Chem Int Ed. 2021; 60: 22075–22080. https://doi.org/10.1002/anie.202103068 PMID: 34288299

85. Farrington GK, Caram-Salas N, Haqqani AS, Brunette E, Eldredge J, Pepinsky B, et al. A novel platform for engineering blood-brain barrier-crossing bispecific biologics. FASEB J. 2014; 28: 4764–4778. https://doi.org/10.1096/fj.14-253369 PMID: 25070367

86. Zheng F, Pang Y, Li L, Pang Y, Zhang J, Wang X, et al. Applications of nanobodies in brain diseases. Front Immunol. 2022; 13. https://doi.org/10.3389/fimmu.2022.978513 PMID: 36426363

87. Dorresteijn B, Rotman M, Faber D, Schravesande R, Suidgeest E, van der Weerd L, et al. Camelid heavy chain only antibody fragment domain against β-site of amyloid precursor protein cleaving enzyme 1 inhibits β-secretase activity in vitro and in vivo. FEBS J. 2015; 282: 3618–3631. https://doi.org/10.1111/febs.13367 PMID: 26147692

88. Marino M, Zhou L, Rincon MY, Callaerts-Vegh Z, Verhaert J, Wahis J, et al. AAV-mediated delivery of an anti-BACE1 VHH alleviates pathology in an Alzheimer's disease model. EMBO Mol Med. 2022; 14. https://doi.org/10.15252/emmm.201809824 PMID: 35352880